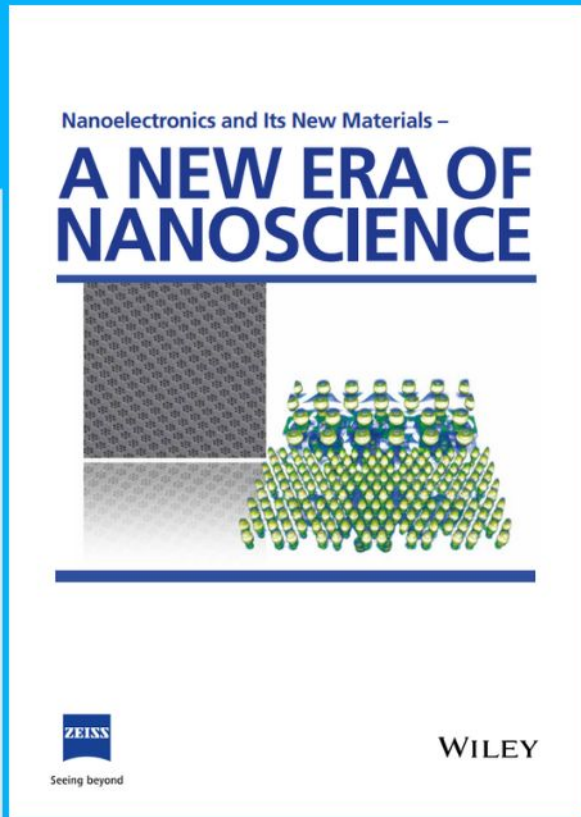




Nanoelectronics and Its New Materials – A NEW ERA OF NANOSCIENCE



Discover the recent advances in electronics research and fundamental nanoscience.

Nanotechnology has become the driving force behind breakthroughs in engineering, materials science, physics, chemistry, and biological sciences. In this compendium, we delve into a wide range of novel applications that highlight recent advances in electronics research and fundamental nanoscience. From surface analysis and defect detection to tailored optical functionality and transparent nanowire electrodes, this eBook covers key topics that will revolutionize the future of electronics.

To get your hands on this valuable resource and unleash the power of nanotechnology, simply download the eBook now. Stay ahead of the curve and embrace the future of electronics with nanoscience as your guide.



Seeing beyond

WILEY

Novel Nanogels Loaded with Mn(II) Chelates as Effective and Biologically Stable MRI Probes

Fabio Carniato, Marco Ricci, Lorenzo Tei, Francesca Garello, Chiara Furlan, Enzo Terreno,* Enrico Ravera, Giacomo Parigi, Claudio Luchinat,* and Mauro Botta*

Here it is described nanogels (NG) based on a chitosan matrix, which are covalently stabilized by a bisamide derivative of Mn-*t*-CDTA (*t*-CDTA = *trans*-1,2-diaminocyclohexane-*N,N,N',N'*-tetraacetic acid). the Mn(II) complex acts both as a contrast medium and as a cross-linking agent. These nanogels are proposed as an alternative to the less stable paramagnetic nanogels obtained by electrostatic interactions between the polymeric matrix and paramagnetic Gd(III) chelates. The present novel nanogels show: i) relaxivity values seven times higher than that of typical monohydrated Mn(II) chelates at the clinical fields, thanks to the combination of a restricted mobility of the complex with a fast exchange of the metal-bound water molecule; ii) high stability of the formulation over time at pH 5 and under physiological conditions, thus excluding metal leaking or particles aggregation; iii) good extravasation and accumulation, with a maximum contrast achieved at 24 h post-injection in mice bearing subcutaneous breast cancer tumor; iv) high T_1 contrast (1 T) in the tumor 24 h post-injection. These improved properties pave the way for the use of these paramagnetic nanogels as promising magnetic resonance imaging (MRI) probes for *in vitro* and *in vivo* preclinical applications.

nearby water molecules, thus modulating signal intensity and contrast enhancement.^[1–3] GBCAs enhance the contrast in all tissues (or organs) where they distribute, leading to great improvements in the diagnosis of even small lesions. Their use is essential for the visualization of small tumor lesions and in the assessment of functional abnormalities. Currently, much attention is devoted to the design of systems with improved properties, reducing the administered dose and finding novel applications. Their efficacy is associated with the ability to vary significantly the T_1 and T_2 nuclear magnetic relaxation times values of tissue water protons in the regions where they are distributed.^[4] A measure of this efficacy is provided by the relaxivity parameter, r_1 , which corresponds to the relaxation rate enhancement of water protons normalized to 1 mM concentration of the paramagnetic metal ion. The relaxivity of MRI CAs used in clinical practice is approximately $4\text{--}5\text{ mM}^{-1}\text{ s}^{-1}$ at 298 K and 1.5 T.^[5]

In recent years, nanoplateforms that function as cargo for the transport of a large number of paramagnetic complexes have attracted a strong interest in the field of molecular MRI.^[6]

1. Introduction

Gadolinium-Based MRI Contrast Agents (GBCAs) are paramagnetic Gd(III) chelates able to increase the ^1H relaxation rate of


F. Carniato, M. Ricci, L. Tei, M. Botta
Dipartimento di Scienze e Innovazione Tecnologica
Università del Piemonte Orientale
Viale T. Michel 11, Alessandria 15121, Italy
E-mail: mauro.botta@uniupo.it

F. Garello, C. Furlan, E. Terreno
Molecular Imaging Centre
Department of Molecular Biotechnology and Health Sciences
University of Torino
Torino 10126, Italy
E-mail: enzo.terreno@unito.it

E. Ravera, G. Parigi, C. Luchinat
Magnetic Resonance Center (CERM)
University of Florence
Sesto Fiorentino 50019, Italy
E-mail: luchinat@cerm.unifi.it

E. Ravera, G. Parigi, C. Luchinat
Department of Chemistry "Ugo Schiff"
University of Florence
Sesto Fiorentino 50019, Italy

E. Ravera, G. Parigi, C. Luchinat
Consorzio Interuniversitario Risonanze Magnetiche Metallo Proteine (CIRMMP)
Sesto Fiorentino 50019, Italy
C. Luchinat
Giotto Biotech S.r.l.
Sesto Fiorentino 50019, Italy

 The ORCID identification number(s) for the author(s) of this article can be found under <https://doi.org/10.1002/smll.202302868>

© 2023 The Authors. Small published by Wiley-VCH GmbH. This is an open access article under the terms of the Creative Commons Attribution License, which permits use, distribution and reproduction in any medium, provided the original work is properly cited.

DOI: 10.1002/smll.202302868

Indeed, the low sensitivity of NMR, intrinsic to the technique, requires the development of signal enhancement procedures if the aim is to target sites and receptors present in low concentrations in biological systems. Nanosystems allow for carrying to the site of interest many paramagnetic metal complexes, most often of Gd(III), lowering the detection limit and thus increasing the sensitivity of the technique. A plethora of nanosized MR probes have been reported in the last 30 years, including paramagnetic chelates embedded in micelles and liposomes, conjugated to nanoparticles (NPs) such as mesoporous silicas and gold NPs or protein-, polymer- and dendrimer-bound structures.^[6–12] In all these systems, each individual paramagnetic chelate experiences a marked decrease in rotational dynamics (increased reorientation correlation time, τ_R) that translates into a significant increase in its r_1 value (r_1 per metal ion). Since there are hundreds or thousands of metal chelates anchored to or incorporated in the nanoprobe, the latter is characterized by an enormous global relaxivity value (r_1 per NP). However, several problems exist for an in vivo translation of these nanosystems. Several characteristics such as size, charge and hydrophobicity have a significant impact on their behavior in vivo, hence nanosized MRI probes must have carefully and finely tuned properties to meet the requirements necessary for biological applications (good compatibility, biodegradability, high relaxivity).

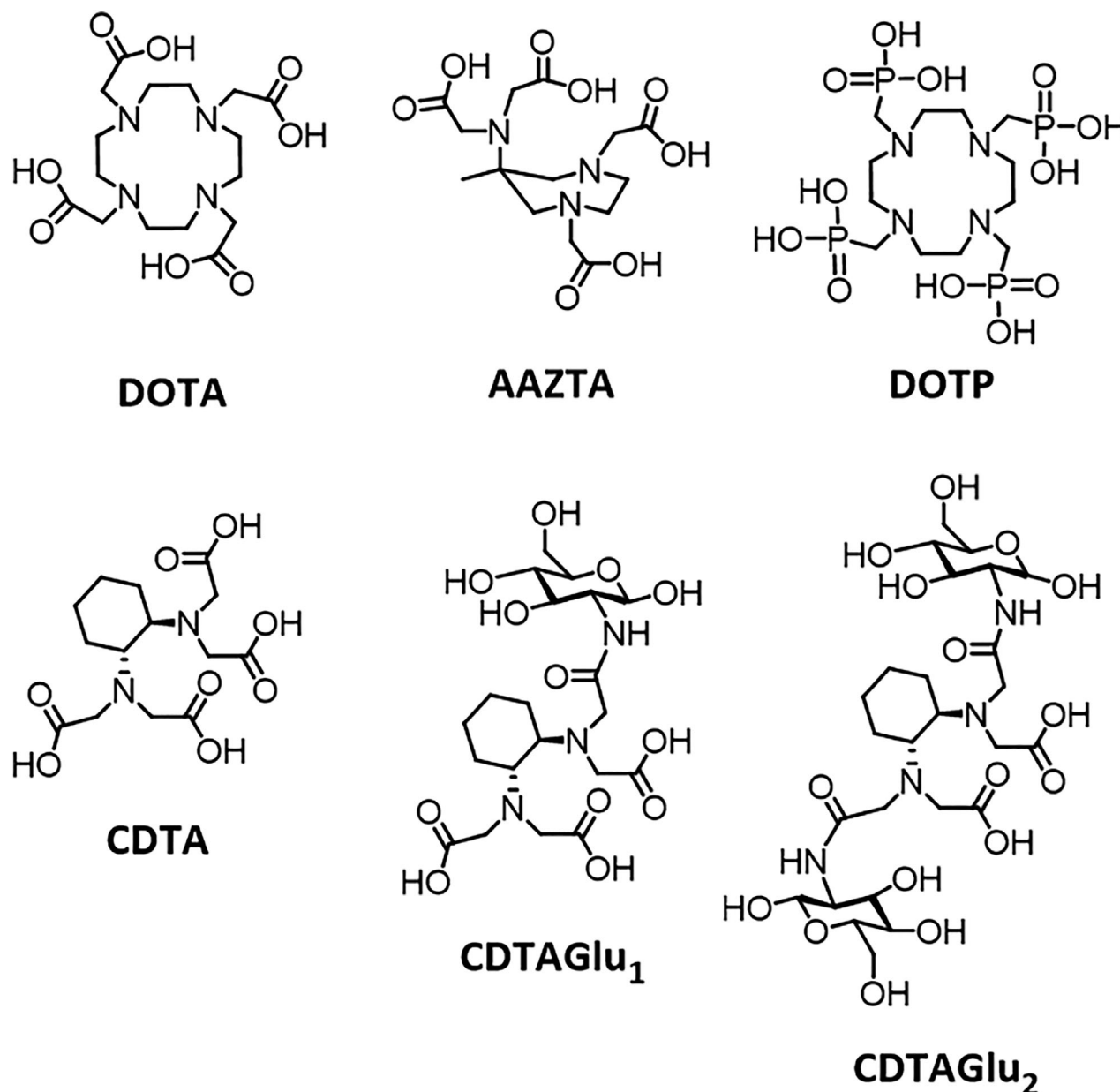
Nanogels formed by non-covalent aggregation of highly biocompatible polymers (e.g.: chitosan, hyaluronic acid, polypeptide-based systems, etc.) and containing Gd(III) complexes incorporated and/or conjugated within the polymeric network are considered a promising novel generation of MRI CA characterized by enhanced sensitivity and improved safety profile.^[13–19] The confinement of GBCAs within nanogels represents a new route to hypersensitive MRI probes. In fact, beside the restriction of the reorientational dynamics related to the encapsulation of the GBCAs, the high water content, the increased viscosity of the water molecules entrapped within the nanosystem, and the presence of an extensive network of hydrogen-bonded proximate solvent molecules can contribute to the relaxivity enhancement. In addition, the confinement of GBCAs within the nanoparticles represents a valuable approach to prevent the unwanted biotransformation of Gd(III)-chelates, including trans-metalation reactions by endogenous metal ions. Stability against biotransformation is crucial for Gd(III)-chelates given the high toxicity of free Gd(III) ions. Recently, we synthesized nanogels (NGs) obtained by electrostatic interactions between biocompatible chitosan and hyaluronic acid and incorporating the Gd(III)-chelates of DOTA (1,4,7,10-Tetraazacyclododecane-1,4,7,10-tetraacetic acid), AAZTA (6-amino-6-methylperh-1,4-diazepine-N'-N''-N'''-tetraacetic acid) and DOTP (1,4,7,10-Tetraazacyclododecane-1,4,7,10-tetra(methylene phosphonic acid) (**Scheme 1**).^[16,18] These complexes differ in coordination geometry, hydration state and overall charge. The paramagnetic NGs exhibit values of $r_1 \approx 10$ –20 times greater than those measured for the isolated complexes, hence demonstrating the validity of the initial hypotheses. Particularly significant is the case of the NGs containing [Gd(DOTP)]⁵⁻ complex that, despite the absence of water molecules coordinated to the Gd(III) ion, shows a remarkable relaxivity value of 78.0 mM⁻¹ s⁻¹ at 20 MHz and 298 K.^[18] However, a recent in vivo MRI study demonstrated

an insufficient stability of [Gd(DOTP)]⁵⁻-incorporating NGs, which resulted in full release of the metal complex within 24 h after its systemic administration.^[18] Therefore, a relevant goal is to find a way to achieve sufficient nanoparticle stability under physiological conditions while maintaining the high relaxivity values measured in vitro. In this work, we present and discuss a possible approach based on the covalent functionalization of NGs with metal complexes.

In general terms, the confinement of paramagnetic chelates in the nanogel matrix can be achieved following two different procedures: 1) physical embedding, based on a network of weak interactions between the metal complexes and the polymeric chains; 2) chemical functionalization of the polymer matrix with chelating agents able to coordinate the paramagnetic metal center. Regarding the first approach, recent studies have shown that chitosan/hyaluronic acid-based nanogels incorporating Gd(III) complexes have insufficient stability under biological conditions.^[18] In the second case, some studies have been carried out on NGs covalently functionalized with Gd(III) chelates or containing paramagnetic ions that act as structural cross-linking agents.^[17,20–22] However, studies of these systems are limited and unsystematic, with rare investigations of their use in vivo as MRI probes. In addition, such nanoparticles showed dimensions greater than 50 nm and relaxivity values at clinical fields lower than those observed for type 1 nanogels.^[22]

It is worth mentioning that some toxicity problems associated with the use of Gd-based contrast agents have been reported in patients with renal insufficiency, who can develop a sometimes fatal disease known as nephrogenic systemic fibrosis (NSF).^[23] In more recent years, the proven long-term deposition of very low amounts of gadolinium in the brain and other tissues has also raised some concerns about the use of this class of contrast agents, especially in the case of multiple administrations.^[24] In addition, the long-term ecotoxicological effects of GBCAs in aquatic environments are also starting to be an issue of concern: the impact of anthropogenic gadolinium is poorly understood and awareness of the need to monitor its distribution and fate in aquatic systems is rapidly growing.^[25] Mn(II)-based systems have been proposed as a potential alternative to Gd(III)-based contrast agents for MRI, due to their potentially lower toxicity and favorable relaxation properties.^[26]

In this work, we propose a new type of chitosan-based nanogel featuring functionalized bisamide-derivatives of *t*-CDTA (*trans*-1,2-diaminocyclohexane-*N,N,N',N'*-tetraacetic acid; **Scheme 1**), a chelate that is known to stably coordinate Mn(II) ions.^[27] Besides avoiding the use of Gd(III) ions, this choice derives from two additional considerations. First, Mn-*t*-CDTA has a water molecule coordinated with the Mn²⁺ ion which ensures relatively high relaxivity values at clinical fields ($q = 1$, $r_1 = 3.6$ mM⁻¹ s⁻¹ at 0.5 T and 298 K),^[27] therefore good contrast ability. Second, the Mn(II) complexes with bisamide derivatives are characterized by high kinetic inertness and good thermodynamic stability, properties that meet the requirements for in vivo MRI applications.^[28] In this contribution, we report the preparation and characterization of the new Mn-based NGs. Remarkably high peak relaxivities of ≈ 30 mM⁻¹ s⁻¹ at 30 MHz is obtained, which are close to record values for Mn-based MRI CAs and are less than a factor of three lower than the best Gd-based MRI CAs. Furthermore, a detailed biological investigation under in vivo and ex vivo conditions was



Scheme 1. Chemical structures of the ligands discussed in this work.

performed to obtain a thorough understanding of the chemical, biological and diagnostic properties of these paramagnetic nanogels.

2. Results and Discussion

2.1. Synthesis and Chemical Characterization

The NG-1 nanogel structure was inspired by a work from Shen et al.^[29] who prepared a biocompatible nanogel made of chitosan and ethylenediamine tetraacetic acid showing a surface switching of both composition and charge in response to pH changes. Thus, NG-1 was synthesized through a covalent cross-

linking reaction of a low molecular weight chitosan (MW = 5000 g mol⁻¹) with a deacetylation degree higher than 90% with *trans*-1,2-diaminocyclohexane-*N,N,N''*-tetraacetic bisanhydride (*t*-CDTA-bisanhydride) (**Figure 1a**). The stoichiometric ratio between chitosan and *t*-CDTA-bisanhydride was 1:70. The nanogel network is stabilized by the presence of amide bonds obtained by reaction of the NH₂ groups of chitosan and the anhydride functionalities of the ligand. The amount of water entrapped in the nanogel matrix was calculated to be 86 wt.% (see experimental section).

Preliminary, the cross-linking reaction was confirmed by infrared spectroscopy: the IR spectra of the nanogel and, for comparison purposes, those of chitosan and *t*-CDTA ligand are shown

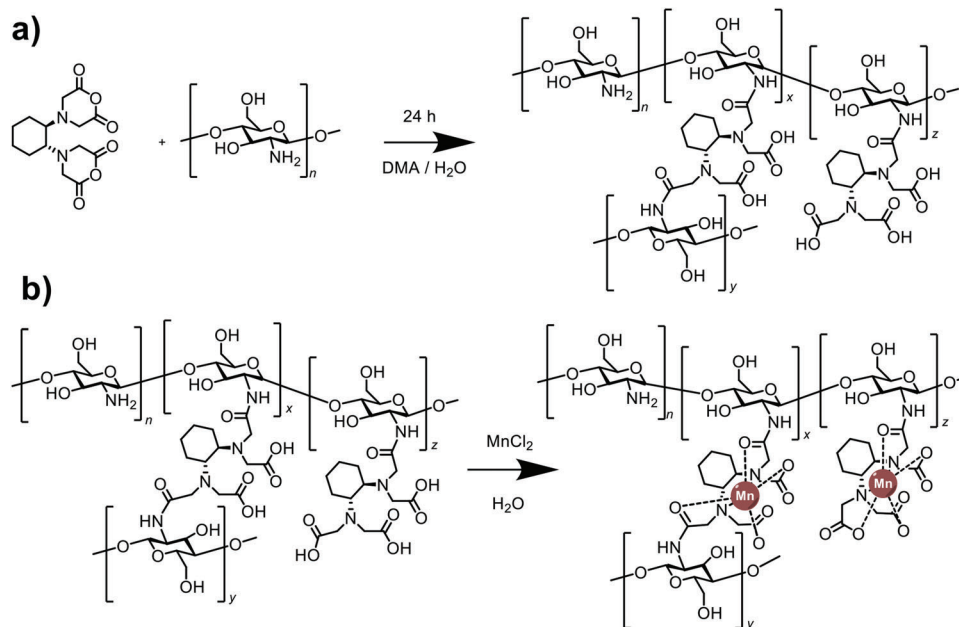


Figure 1. Schematic illustration of the synthesis of NG-1 matrix (a) and of the coordination with Mn(II) ion (b).

in **Figure 2**. The peak 1735 cm^{-1} , attributed to the stretching modes of the free carboxylic groups of *t*-CDTA, and the absorptions at 1635 and 1555 cm^{-1} , assigned to the stretching and bending of the CO and NH groups of the amide bond, are a proof of the attachment of *t*-CDTA-bisanhydride to the chitosan chains. This

result is also supported by a quantitative evaluation of the functionalization degree of the chitosan after reaction with *t*-CDTA-bisanhydride by using ninhydrin test, a standard procedure for the quantification of free NH₂ groups.^[30] By the analysis of the absorbance of the band at 590 nm , generated by the reaction of

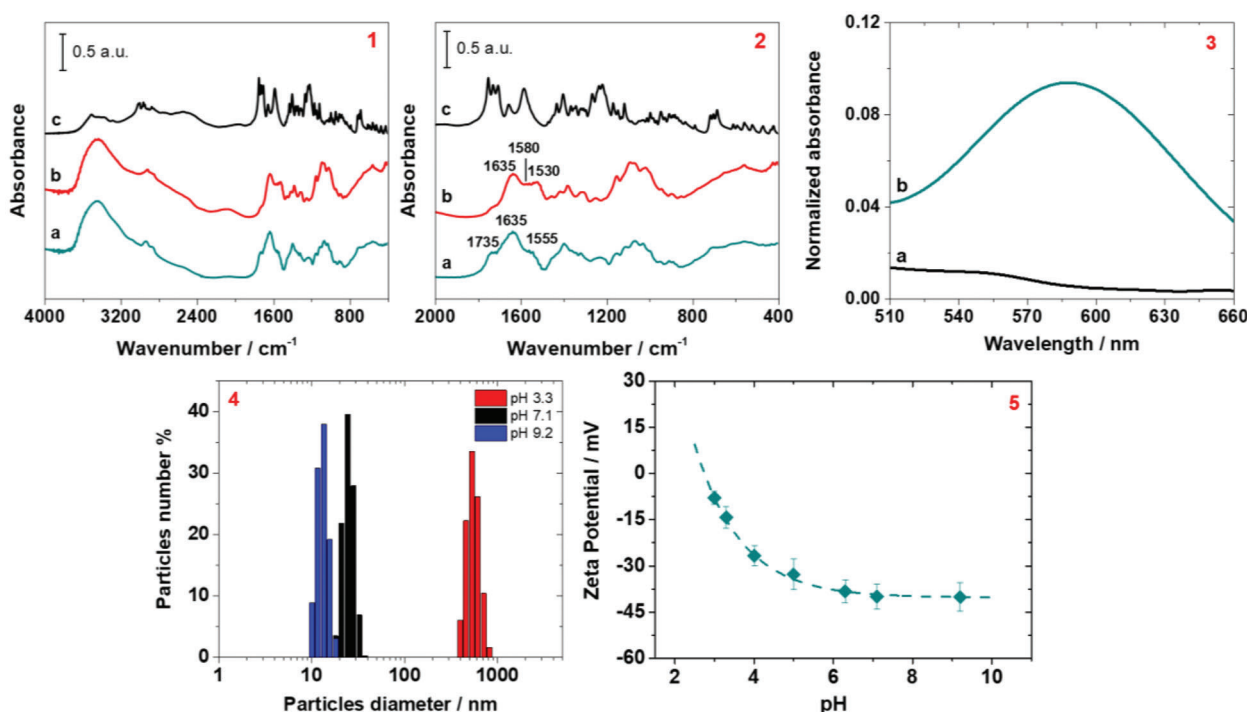


Figure 2. 1) IR spectrum in KBr matrix of NG-1 (a), chitosan (b) and *t*-CDTA anhydride (c); 2) magnification of the IR spectra in the 2000–400 cm⁻¹ range; 3) UV-vis spectrum of ninhydrin solution before (a) and after mixture with NG-1 (b); 4) DLS data of NG-1 suspension at pH 3.3 (red), 7.1 (black) and 9.2 (blue); 5) Z-potential values of NG-1 as a function of pH (the points represent the mean value and the error bars indicate the standard deviation; $n = 3$).

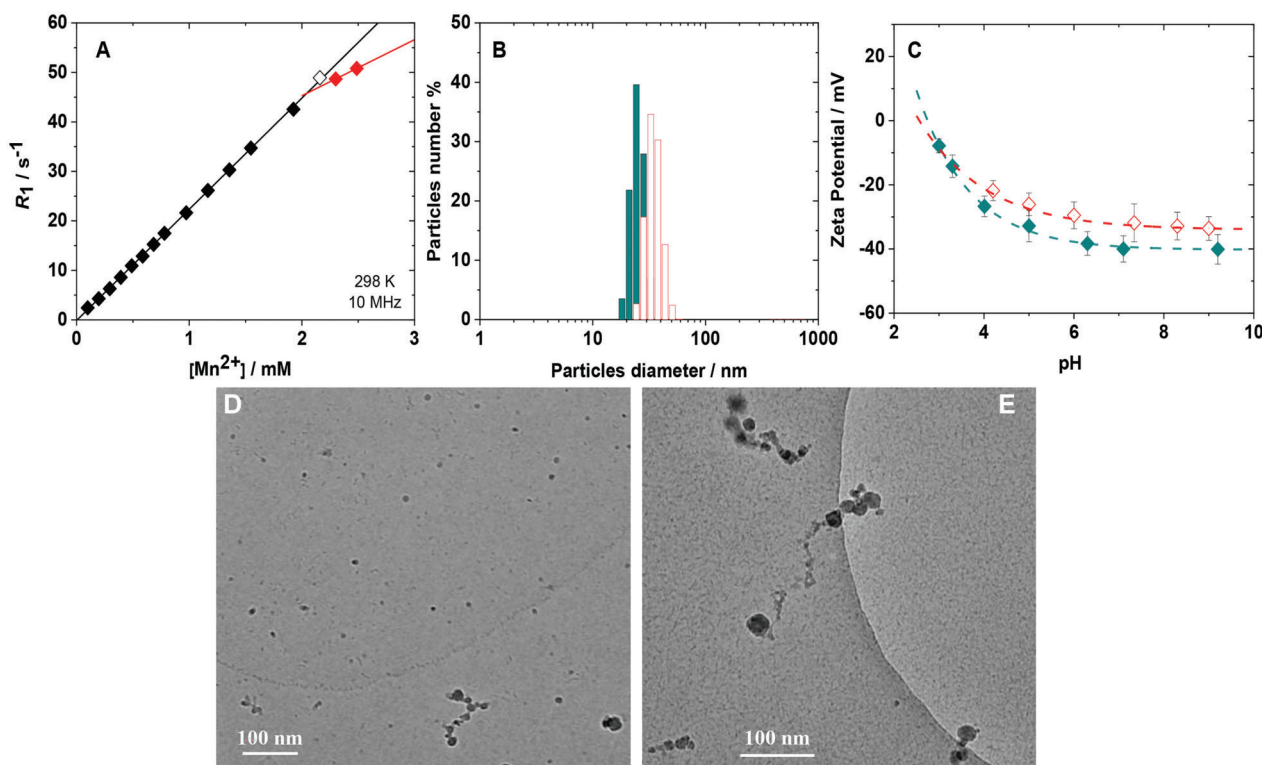


Figure 3. A) values of ^1H R_1 (10 MHz) of a suspension of NG-1 in aqueous solution at pH = 4.5 and 298 K as a function of increasing additions of Mn(II); B) particles size distribution in aqueous solution of NG-1 (green) and Mn-NG-1 (red) at physiological pH; C) Z-potential values as a function of pH of Mn-NG-1 (red) as compared to NG-1 (green); (the points represent the mean value and the error bars indicate the standard deviation; $n = 3$). Cryo-TEM micrographs of Mn-NG-1 at low and high magnifications are reported in (D) and (E), respectively.

ninhydrin with the free NH_2 groups of chitosan (Figure 2 (3)), it is possible to conclude that 34% of amino functionalities were involved in the reaction with *t*-CDTA-bisanhydride. In this regard, it is important to note that the reaction of *t*-CDTA-bisanhydride with chitosan can give rise to two different products: 1) both anhydride groups react with two primary amines of two adjacent chitosan chains to form a bis-amide derivative of *t*-CDTA and favoring the cross-linking and the gelation reaction; 2) one anhydride reacts with the amino group of a single saccharide unit of chitosan while the other anhydride is hydrolyzed by water molecules to form a monoamide derivative of *t*-CDTA (Figure 1).

The morphological properties of NG-1 in aqueous suspension, after purification through dialysis, were examined by DLS analysis as a function of pH. At basic pH (pH = 9.2), the hydrodynamic diameter of the nanoparticles is ≈ 15 nm with a narrow size distribution (PDI = 0.02) (Figure 2 (4)). The suspension appeared stable and homogenous without visible sedimentation. This is explained considering the high Z-potential value (-40 mV), originating from the presence of the free carboxylate groups of *t*-CDTA exposed on the particles surface (Figure 2 (5)). A similar behavior was observed also at physiological pH (pH = 7.1), where the suspension is composed of particles with an average hydrodynamic diameter of 25 nm (PDI = 0.01) and a Z-potential of -39 mV. At pH 3.3, we observed a switch of the nanogel surface, in agreement with the behavior previously observed for chitosan-EDTA nanogels,^[29] which involves the partial protonation of the carboxylic groups of *t*-CDTA and an exposure

on the surface of the positive ammonium groups of the chitosan component (Figure 2 (5)). This switch induces an increase of the Z-potential up to -10 mV and an increment of the average hydrodynamic diameter centered to ≈ 600 nm and the aggregation of the particles that gives rise to flocculation (Figure 2 (4)).

The modification of the functional groups exposed on the particles surface was also confirmed by ^1H NMR spectroscopy. The proton NMR spectrum of NG-1 dissolved in D_2O at pH 2 shows the characteristic peaks of the protonated chitosan in the 3.6–3.9 ppm range.^[29] At neutral pH, the signals of negatively charged *t*-CDTA become dominant (narrow peaks at 3.5 and 3.7 ppm) with respect to those of chitosan, suggesting that the negative groups of the ligand are mainly exposed on the external surface of the nanogel matrix (Figure S1, Supporting Information).

The NG-1 suspension was then treated with a MnCl_2 solution (48.4 mM) at pH 4.5 and 298 K to promote the coordination of Mn(II) by the *t*-CDTA mono- and bisamide ligands and the complexation reaction was monitored through ^1H NMR relaxometry (Figure 3). In detail, the water protons longitudinal relaxation rate (R_1) of the NG-1 suspension was measured at 10 MHz and 298 K as a function of increasing amount of Mn^{2+} ions, resulting in a linear trend as shown in Figure 3A. A small excess of Mn(II) over the molar concentration of the ligand induces a marked change in the slope of the line (Figure 3A). The metal excess can be easily complexed with a small amount of NG-1 suspension (20 μL).

The resulting paramagnetic Mn-NG-1, in aqueous solution at neutral pH, showed particles size distribution with

Table 1. Comparison of the morphological and chemical properties of the three NG formulations.

	Particles diameter [nm]	Zeta potential [mV]	Suspension stability	Functionalization degree of chitosan
NG-1	25	-39	High	34%
NG-2	380	-35	Fast particles sedimentation	51%
NG-1/3	6	-38	High	23%

hydrodynamic diameter of ≈ 30 nm, a value comparable to that observed for NG-1 (Figure 3B). The particles size was also evaluated by cryo-TEM analysis. The images at low and high magnifications (Figure 3D and E, respectively) show that Mn-NG-1 is composed by particles of spheroidal morphology and diameter ≈ 20 nm. Furthermore, the pH-dependence of the Z potential values is very similar to that measured for NG-1, with slightly fewer negative values due to the presence of the coordinated Mn(II) (Figure 3C).

The Mn(II) concentration of the Mn-NG-1 suspension was 2.16 mM (1.35 mmol g^{-1}), corresponding to $\approx 3400 \text{ Mn}^{2+}$ ions per particle (more details on the procedure used for Mn^{2+} quantification is reported in the supporting material, ESI). The metal loading and the morphological properties of the nanogel can be modulated by changing the molar ratio between the ligand and the chitosan in the synthetic procedure. Other two nanogels were prepared using in one case a double quantity of *t*-CDTA-bisanhydride (NG-2) and in the other a quantity equal to one third (NG-1/3). Both samples were fully characterized (Table 1 and Figure S2, Supporting Information). The NG-2 suspension is composed by particles with an average hydrodynamic diameter centered at 380 nm (PDI = 0.02), which tends to precipitate over time (Table 1 and Figure S2, Supporting Information). This behavior is associated with a higher functionalization degree of the amino groups of chitosan involved in the reaction with *t*-CDTA-anhydride, close to 51% as estimated by the ninhydrin test (Figure S3, Supporting Information). The high instability of this suspension makes this formulation unsuitable for biological ap-

plications. On the other hand, NG-1/3 shows a particles size distribution in aqueous solution with a maximum at 6 nm (PDI = 0.11) at neutral pH, ca. three times lower than that of NG-1, but with a functionalization degree of the chitosan matrix of only 23% (Table 1). Furthermore, the Mn(II) concentration of the paramagnetic derivative Mn-NG-1/3 suspension is 1.04 mM, a value less than half that of the Mn-NG-1 formulation. For these reasons, Mn-NG-1 appears to combine the best characteristics for diagnostic applications, such as particles size, stability of the suspension and Mn^{2+} loading.

2.2. Relaxometric Characterization

At 298 K, the observed r_1 of Mn-NG-1 at 30 and 60 MHz (0.75 and 1.45 T, respectively) assumes the values of 29.2 and $16.3 \text{ mM}^{-1} \text{ s}^{-1}$ (calculated per Mn(II) ion), respectively. These values are up to seven times higher than those typical for Mn(II) chelate monohydrates, measured under identical conditions (Figure 4).^[26] This result is a clear indication that Mn(II) ions have been stably and effectively incorporated into NGs, where they are characterized by restricted rotational dynamics (long τ_R) and a sufficiently high rate of coordinated water exchange, k_{ex} . Under these conditions, paramagnetic nanosystems typically show r_1 values that have a peak centered around 30–50 MHz.

The relaxivity of Mn-NG-1 was measured at different pH values to evaluate the chemical stability of the chelates, covalently incorporated within the nanogel network (Figure 5A). Interestingly, the r_1 value measured at 30 MHz and 298 K remains constant over the pH range 4 to 10. This indicates that the hydration state of the metal does not change with pH and that hydrolysis or aggregation phenomena do not occur. Furthermore, the stability of the formulation was evaluated by monitoring the value of r_1 as a function of time, over a period of two weeks, at pH 5 and 7.4 (Figure 5B). The relaxivity of the suspension remains constant over the entire time interval, indicating the lack of release of metal ions from the NGs and/or the absence of nanoparticle aggregation. The suspension stability was also monitored by measuring particle size distribution and surface charge by DLS analysis over time at pH 7.4. Both the hydrodynamic diameter

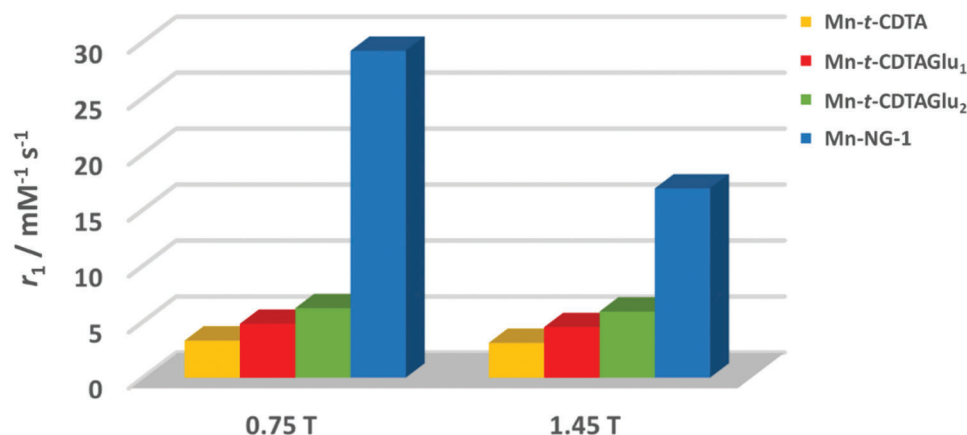


Figure 4. Comparison of r_1 values at 0.75 and 1.45 T (298 K) for Mn-*t*-CDTA, its mono- and bisamide derivatives, and for Mn-NG-1.

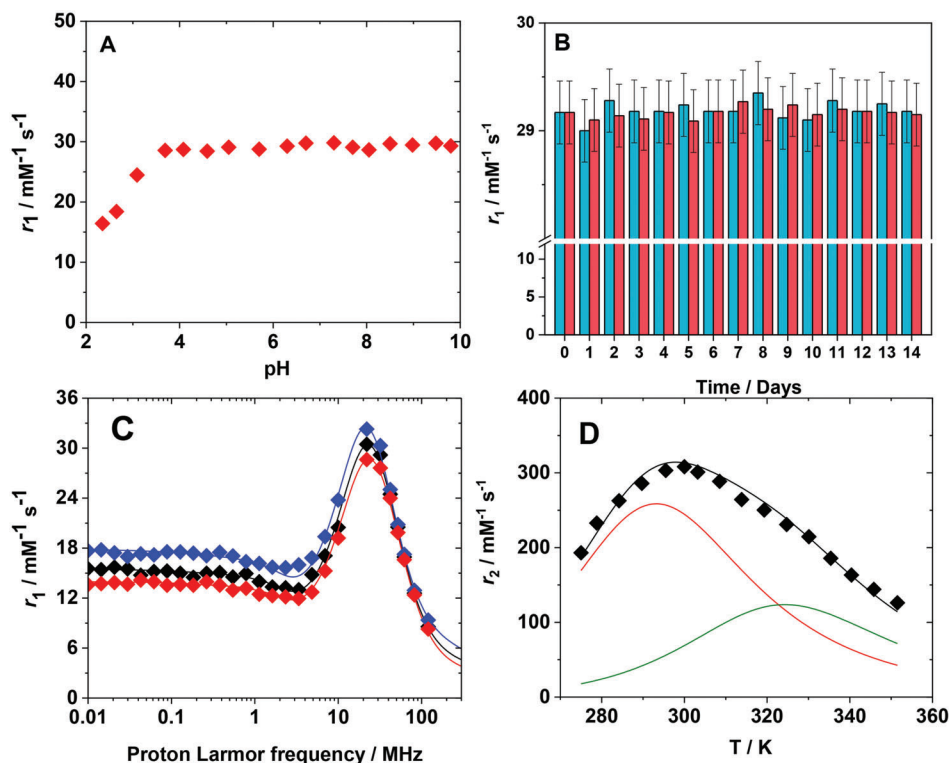


Figure 5. A) pH dependence of the relaxivity for Mn-NG-1 at 298 K and 30 MHz; B) stability test over time at pH 5 (red) and 7.4 (blue) of Mn-NG-1 (the bars represent the mean value and the error bars indicate the standard deviation; $n = 3$); C) ^1H NMRD profiles Mn-NG-1 at 283 (blue), 298 (black) and 310 K (red) at neutral pH; D) ^{17}O transverse relaxation rates as a function of temperature of Mn-NG-1 ($[\text{Mn}^{2+}] = 1.8 \text{ mM}$) at neutral pH, at 11.7 T. The solid line corresponds to the best-fit of the data. Red and green lines represent the contributions of the two different Mn(II) sites with different water exchange rates.

distribution and the Z potential values show no appreciable change over a two-week period, thus confirming the good stability of the suspension (Figure S4, Supporting Information). At lower pH ($\text{pH} < 4$), the relaxivity progressively decreases because of the gradual and reversible acid-activated metal complex dissociation process (Figure 5A).

The ^1H longitudinal relaxivity (r_1) of Mn-NG-1 in a diluted aqueous suspension was measured as a function of temperature (283, 298 and 310 K) over the proton Larmor frequencies range 0.01 – 120 MHz. The data, in the graphical form of Nuclear Magnetic Relaxation Dispersion (NMRD) profiles, are shown in Figure 5C. The ^1H NMRD profiles confirm the presence of a well-defined peak centered ≈ 30 MHz, typical of slowly tumbling paramagnetic systems with a reorientational correlation time (τ_R) much longer than the electronic relaxation time.^[5] The Mn(II)-chelate units are linked to the chitosan chains and thus possess a limited degree of rotational freedom in solution. The profiles were analyzed using the Florence NMRD model,^[31] which considers the presence of both static and transient zero-field splitting (ZFS), as well as the presence of internal mobility through the Lipari-Szabo model-free approach.^[32] The fitted profiles reproduce the experimental data very well (see Figure 5C), with the parameter values reported in Table 2.

The relaxivity values measured at different applied magnetic fields increase with decreasing temperature, as expected for paramagnetic systems with relaxivities that are not limited by the rate of water exchange k_{ex} . This qualitative information is supported

Table 2. Parameters obtained from the analysis of the ^1H NMRD profiles of Mn-NG-1 using the Florence NMRD model. Best fit values of τ_R and τ_M are reported for the cases of single (I) or double (II) species.

	283 K	298 K	310 K	
q^{a}		1		
ρ^{a}		2.83		Å
Δ_t		0.019		cm^{-1}
τ_v	47	43	41	ps
τ_{fast}	230	155	115	ps
S^2		0.36		
ZFS, angle		0.014 cm^{-1} , 55°		
I. τ_R	5.0	4.4	4.2	ns
τ_M	83	38	22	ns
II. τ_R	5.2	4.7	4.6	ns
τ_M^{A} (69%) ^{a)}	39	19	11	ns
τ_M^{B} (31%) ^{a)}	183	83	47	ns

^{a)} Fixed value. Distance of closest approach of freely diffusing water molecules and diffusion coefficients were fixed to 3.25 Å and to 1.5, 2.3 and $3.0 \times 10^{-9} \text{ m}^2 \text{ s}^{-1}$ at 283, 298 and 310 K, respectively.

by high resolution ^{17}O NMR experiments, which provide accurate values of the exchange rates and the associated activation parameters of inner-sphere water molecules. Variable temperature transverse ^{17}O NMR relaxation rates (R_2) were recorded at 11.7 T

on a 1.8 mM solution of Mn-NG-1 in ^{17}O -enriched water. The experimental data were then analyzed using the well-established Swift-Connick equations.^[33] The transverse relaxation rates increase as the temperature decreases, reaching a maximum at ≈ 300 K and then decreasing at lower temperatures (Figure 5D). This bell-shaped pattern resembles that characteristic of intermediate exchange regime systems.^[5] However, the curve deviates from the typical trend and, especially at $T > 310$ K, the decrease in R_2 values is less than expected. In fact, fitting the data to the Swift-Connick equations does not produce an acceptable result.

This suggests that the anomalous temperature dependence of the ^{17}O R_2 values can be attributed to the presence of two different species characterized by a different exchange regime. These two components (A and B) differing in the water exchange dynamics can be explained considering the distribution of mono- and bisamide Mn-*t*-CDTA units covalently linked to the chitosan polymer (Figure 1). This effect is well known in the case of Gd(III) complexes. The decrease in the negative charge of the complex by one (monoamide; A) or two (bisamide; B) units leads to an increase in the metal-water interaction, and therefore the removal of the water molecule from the coordination site is associated with a greater enthalpy barrier.^[34] In fact, the experimental data were nicely reproduced (Figure 5D) on the basis of a model that considers the presence of two monohydrate species that differ in the average exchange lifetime ($\tau_M^A = 19$ ns and $\tau_M^B = 83$ ns) and in the corresponding activation enthalpy values ($\Delta H_M^A = 34$ kJ mol $^{-1}$ and $\Delta H_M^B = 37$ kJ mol $^{-1}$). The molar fraction of the A and B Mn(II) sites is 0.69 and 0.31. It is remarkable that the best fit values of τ_M obtained from the fit of the ^1H relaxivity profiles in Figure 5C are in excellent agreement with the weighted averages of τ_M^A and τ_M^B .

The ^1H relaxivity profiles in Figure 5C were also analyzed by fixing the two values of τ_M^A and τ_M^B obtained for the two species, with the corresponding weights, and the parameters reported in Table 2. The profiles are not appreciably different from those calculated with a single τ_M , shown in Figure 5C. The electron relaxation parameters obtained from the fit are the transient ZFS (Δ_{ν} , of 0.019 cm $^{-1}$), the correlation time for electron relaxation (τ_{ν} , of ≈ 40 ps), and the static ZFS of 0.014 cm $^{-1}$. Fixing the values of τ_M also permitted to remove any covariance with the reorientation correlation time τ_R , which resulted of several nanoseconds. This value is much higher than the value for a small Mn(II)-complex, as expected, but smaller than the overall reorientation time of the nanogel particle. This finding points to the presence of extensive internal mobility, which is also suggested by large contributions from even faster correlation times, of the order of hundred picoseconds. This finding is also in line with what previously observed for Gd-complexes embedded in similar nanogel matrices.^[16] Noteworthy, τ_R values much shorter than expected from rigid reorientation have been found for many nanosized systems,^[35–39] suggesting that the occurrence of internal structural rearrangements of particle regions can be a common phenomenon.

To find further support for the hypothesis of the presence of two monohydrate species differing in the exchange lifetime, two new Mn(II) complexes, Mn-*t*-CDTAGlu $_1$ and Mn-*t*-CDTAGlu $_2$ (Scheme 1 and Figure S5, Supporting Information), whose structure is strictly related to A and B species linked to the chitosan chains, were synthesized by reacting-CDTA-bisanhydride with

Table 3. Water exchange parameters and hyperfine coupling constant obtained from simultaneous fit of the ^1H NMRD and ^{17}O NMR data for the different Mn(II) species.

Parameter	Mn- <i>t</i> -CDTAGlu $_1$	Mn- <i>t</i> -CDTAGlu $_2$	Mn-NG-1 Fraction A	Mn-NG-1 Fraction B
τ_M^{298} / ns	23	36	19	83
ΔH_M / kJ mol $^{-1}$	31	28	34	37
A_O/\hbar / 10 6 rad s $^{-1}$	-25.0	-26.2	-25.0	-26.0

glucosamine. The two ligands were then purified by semi preparative HPLC-MS and fully characterized by ^1H and ^{13}C NMR spectroscopy (ESI). The ^1H NMRD profiles of both chelates were collected at 283, 298 and 310 K (Figure S6, Supporting Information). Moreover, the ^{17}O reduced transverse relaxation rates (R_{2r}) and chemical shift ($\Delta\omega_c$) data were measured over the same temperature range of Mn-NG-1 (Figure S7, Supporting Information). We have assumed that both complexes are monohydrates ($q = 1$), in analogy with the parent complex $[\text{Mn}(t\text{-CDTA})(\text{H}_2\text{O})]^-$. This hypothesis is fully consistent with the NMRD profiles that are typical of small Mn(II) monohydrate complexes. Furthermore, the hydration state of the Mn $^{2+}$ ion can be estimated using an empirical relationship correlating q , the relaxivity value at 0.01 MHz and 298 K, and the molar mass of the complex.^[40]

$$q = \frac{r_1 (0.01 \text{ MHz})}{9.16 \left\{ 1 - e^{(-2.97 \times FW \times 10^{-3})} \right\}} \quad (1)$$

The uncertainty of q estimated with this method is equal to ± 0.4 . The calculated q values for Mn-*t*-CDTAGlu $_1$ and Mn-*t*-CDTAGlu $_2$ are 0.91 and 0.98 respectively, thus confirming our assumption. All the data were simultaneously analyzed in terms of the well-established equations for the inner- and outer sphere proton relaxation mechanisms and of the Swift-Connick equations. An excellent fit of the ^1H NMRD and ^{17}O NMR data was obtained with the parameters listed in Table 3 and Figure S1 (Supporting Information).

The τ_M values for Mn-*t*-CDTAGlu $_1$ and Mn-*t*-CDTAGlu $_2$ are similar to those calculated for the two species A and B of Mn-NG-1. The exchange of the coordinated water molecule is quite fast ($\approx 3 \times 10^7$ s $^{-1}$) and therefore such as not to influence their relaxivity, which is largely controlled (especially at high fields) by the rotational dynamics (τ_R) (Figure 6). Unexpectedly, the k_{ex} values between the two complexes differ less than that found in the case of analogous Gd(III) complexes. Probably, the change in electric charge passing from the mono- to the bisamide CDTA derivative is well compensated by the increase in the steric hindrance around the coordination site of the water molecule, which favors the exchange process. This effect is more visible at low temperatures where the exchange process slows down further. In fact, by lowering the temperature in the range of 320–275 K, relaxivity increases only slightly and reaches a plateau ≈ 290 K (Figure S8, Supporting Information). In this region, water exchange markedly limits relaxivity and the system transitions from an intermediate to slow exchange regime (Table 3).

In order to assess the suitability of these nanoprobe for biological analyses, a stability test of the Mn-NG-1 suspension

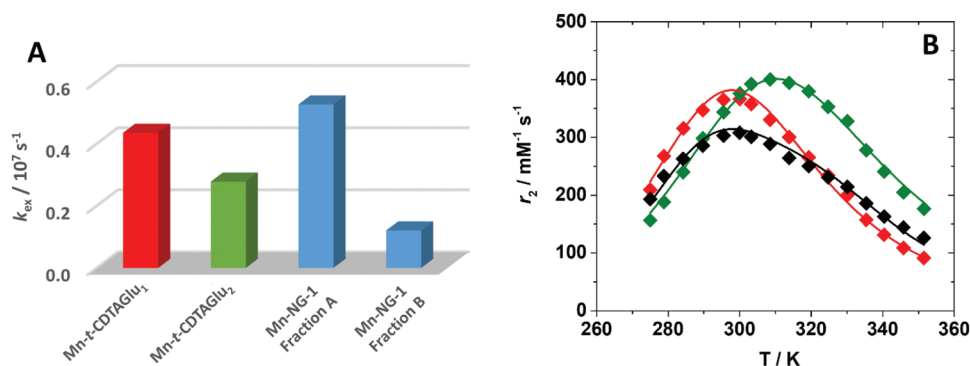


Figure 6. A) Water exchange rate (k_{ex}), calculated by ^{17}O NMR data, for Mn-NG-1, Mn-t-CDTAGlu₁ and Mn-t-CDTAGlu₂; B) Comparison of ^{17}O r_2 as a function of temperature for Mn-NG-1 (\blacklozenge), Mn-t-CDTAGlu₁ (\blacklozenge) and Mn-t-CDTAGlu₂ (\blacklozenge).

was carried out in the presence of reconstituted human serum (SeronormTM). The solution was prepared by dissolving 90 mg of Seronorm in 1 mL of the Mn-NG-1 suspension. The ^1H -NMRD profiles collected on Mn-NG-1 dispersed in pure water and in Seronorm at physiological pH and 310 K exhibit identical shapes and amplitudes (relaxation rates) over a 24 h period. This suggests that the nanoparticles maintain their integrity even when dispersed in biological fluids, without interactions with the biomolecules contained in the matrix and/or the release of free Mn(II) ions. (Figure S9, Supporting Information).

2.3. Biological Characterization

The biocompatibility of Mn-NG-1 was tested on the macrophage cell line RAW 264.7. The MTT assay performed 24 h after the incubation of the cells with increasing amounts of Mn-NG-1 proved the absence of cytotoxic effects (Figure S10, Supporting Information). Subsequently, Mn-NG-1 was injected intravenously in healthy BALB/c mice to determine their blood half-life time. Soon after the injection, micro-aliquots of blood were collected at different time points and mineralized to quantify the Mn(II) content. Results obtained were fitted with a biexponential decay model ($R^2 = 0.986$), resulting in a faster component with a half-life of 22 min, followed by a slower component with a half-life of ≈ 5 h (Figure 7). This behavior is quite commonly observed for the clearance of nanoparticles from the bloodstream, and in line with other reported data.^[41,42]

Mn-NG-1 was then tested in mice bearing a subcutaneous breast cancer tumor, to investigate their ability to extravasate into the tumor and originate an MRI-detectable contrast enhancement in the lesion. For this purpose, the nanosystem was diluted in HEPES/NaCl buffer to obtain an isotonic suspension (300 mOsm, 2 mM Mn(II)), which was intravenously injected (13 μmol Mn(II)/kg). The dosage employed was comparable with that of other manganese-based contrast agents (e.g., TeslascanTM 5–10 μmol kg⁻¹, though higher dosages, up to 100 μmol kg⁻¹, were reported).^[43–45] The % T_1 -SE values (at 1 T) measured in the tumor demonstrated good extravasation and accumulation of the nanoparticles, due to the well-known enhanced permeability and retention (EPR) effect,^[46] with a maximum contrast achieved at 4 h post-injection (p.i.), slowly decreasing at 48 h p.i. (Figure 8A). The MRI data about the biodistribution of the nanosystem dis-

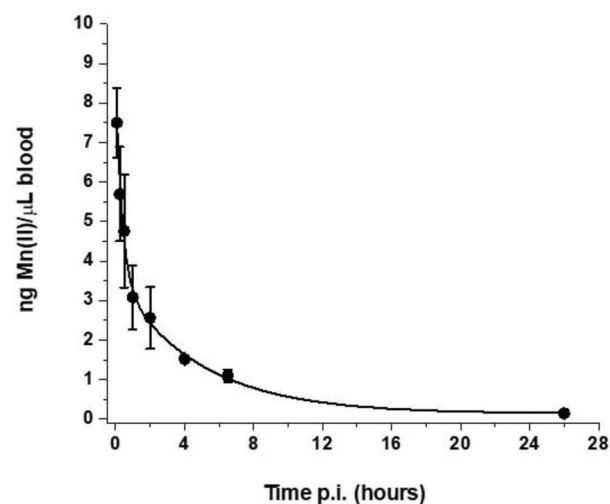


Figure 7. Time-dependent Mn(II) concentration in blood, calculated as ng Mn(II)/ μL blood, at different time points post intravenous injection of Mn-NG-1 in healthy balb/c mice ($n = 3$, $R^2 = 0.986$) (the points represent the mean value, and the error bars indicate the standard error of the mean; $n = 3$).

played a steep increase of the T_1 contrast in the spleen at 30 min, with a rapid decrease in the following hours (Figure 8B). In the liver, the contrast remained almost unchanged until 4 h p.i., and then started to decrease at 24 and 48 h p.i. The quite high T_1 contrast observed both in the liver and spleen can be attributed to the typical nonspecific uptake of the nanomaterials by the reticuloendothelial system (RES) organs, containing resident phagocytic cells such as monocytes and macrophages.^[47–49] Finally, a well-detectable contrast was measured also in the kidneys. Representative MRI T_{1w} and T_{2w} images of all the investigated organs, acquired before and at different times post-injection, are reported in Figure 8C.

To confirm the in vivo data, ICP-MS analysis of the explanted organs was performed 24 h post-injection to quantify the amount of Mn(II) ions (Figure 9). At variance with what observed by MRI, where the T_1 contrast in the organs at 24 h p.i. was similar, the Mn(II) content per gram of tissue was quite different among the examined organs. The amount of Mn(II) found in the spleen was the highest (≈ 30 times higher than the basal content), followed by

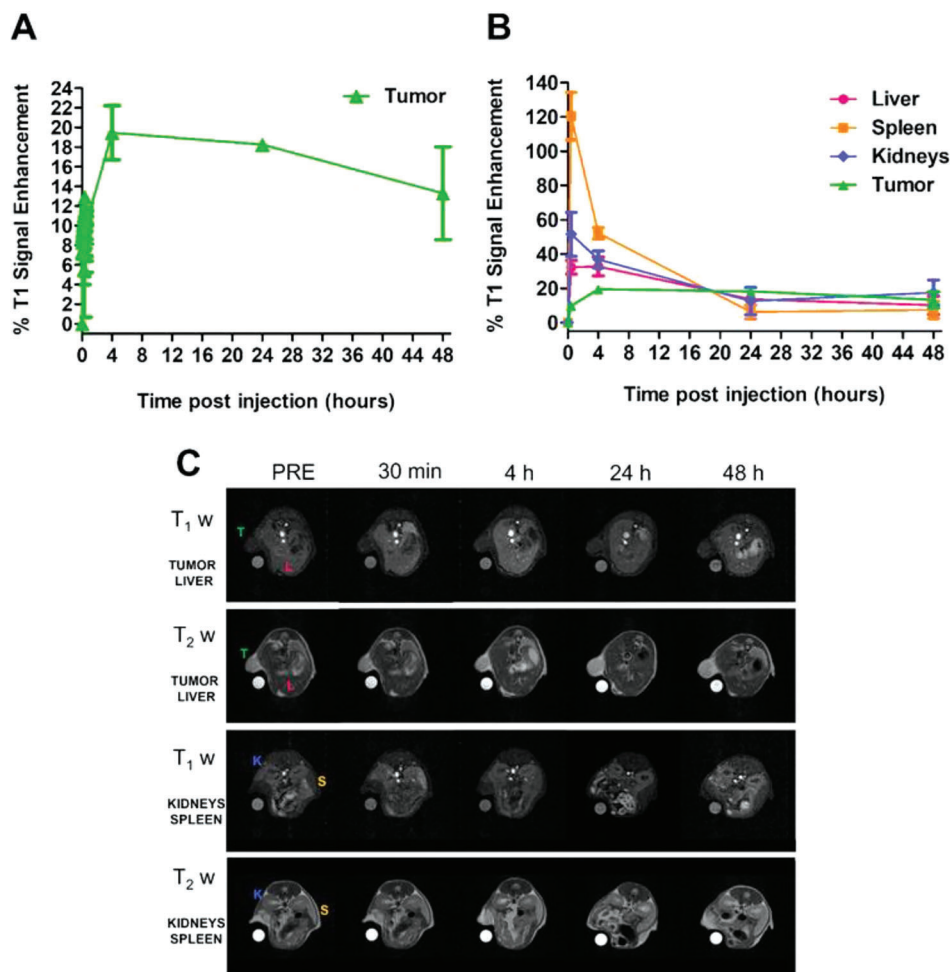


Figure 8. % T₁ SE measured A) in the tumor only and B) in the liver, spleen, kidneys, and tumor at different time points post intravenous injection of the Mn-NG-1 sample (the points represent the mean value, and the error bars indicate the standard error of the mean; $n = 3$). C): Representative MRI T_{1w} and T_{2w} images of tumor (T), liver (L), kidneys (K), and spleen (S) acquired at 1 T before and at different times post-injection of the nanogels.

the liver (≈ 9 times higher than the basal value), tumor (20 times higher), and kidneys (3.5 times higher).

The Mn(II) uptake could be associated with the content of phagocytic cells in the examined tissues. Spleen and liver are main organs of the Mononuclear Phagocytic System and contain a much higher number of phagocytic cells that are known to be the main responsible for the uptake of nanosystems.^[49] Likely, the intracellular fate of the nanogel taken up by phagocytic cells causes a degradation of the nanogel that generates paramagnetic species (e.g., the Mn-*t*-CDTA-like complexes) with relaxivity values much lower than the intact nanogel. However, the observation that in the tumor the T₁ contrast at 24 h post-injection is like that in the other organs despite a much lower amount of Mn(II) is a promising finding for the potential applications of this system in cancer imaging.

3. Conclusion

We have rationally designed and prepared new paramagnetic nanogels in which the metal ion coordination cage is covalently linked to the chitosan structure. This procedure yields consider-

ably more stable nanoparticles with respect to the previous examples where the metal complexes were simply incorporated into the nanogels. In these previously reported systems, we observed a rapid release of metal chelate cargo in biological fluids. On the contrary these new NGs stably retain the metal chelate and allowed us to perform *in vivo* MRI studies on animal models. Indeed, this optimized design is based on a number of considerations and knowledge accumulated over several years. We first decided to develop nanoprobcs based on Mn(II), a metal ion that has a better toxicity profile than Gd(III) and a lower long-term environmental impact. To this end, we have used bisamide derivatives of CDTA to incorporate such chelators into the chitosan structure, because recent studies evidenced a pronounced kinetic inertness of these Mn(II) complexes. The complexation of Mn(II) ions occurs rapidly and completely and the resulting nanogels are stable both in aqueous solution and in biological fluids. A comprehensive ¹H and ¹⁷O NMR relaxometric study of nanoprobcs and model mononuclear complexes clearly confirmed that the Mn(II) ion is monohydrate and in a fast exchange regime. This property is essential to maximize the effectiveness of the probes (relaxivity).

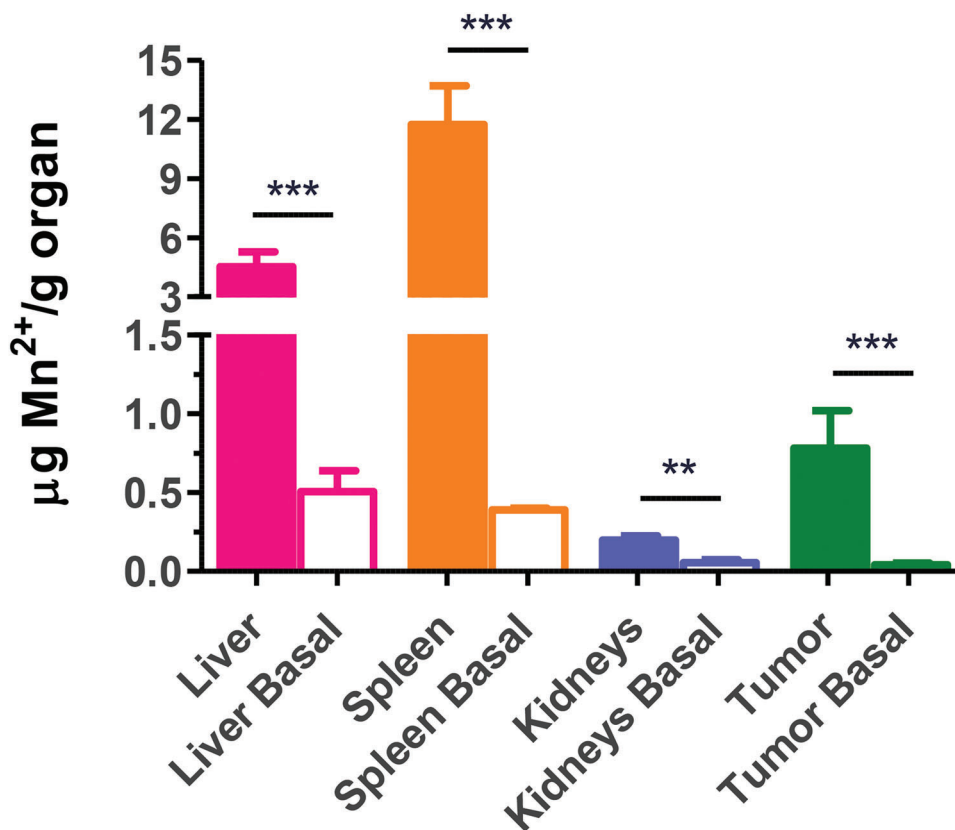


Figure 9. ICP-MS quantification of Mn(II) in liver, spleen, kidneys, and tumor determined in control TS/A tumor-bearing mice (basal, $n = 3$) and in TS/A tumor-bearing mice treated with Mn-NG-1 nanogel, sacrificed 24 h p.i. ($n = 3$). The bars represent the mean values and the error bars indicate the standard deviation; $n = 3$. Statistical analysis: two-tailed t-student test (** $p < 0.01$, *** $p < 0.001$).

Table 4. r_1 values (per Mn; 0.5 T / 1.5 T and 298 K) of Mn-NG-1 and selected nanoparticles functionalized with different Mn(II) chelates.

Nanoparticles	$r_1 / \text{mm}^{-1} \text{s}^{-1}$ at 298 K (0.5 T / 1.5 T)	Ref.
HCDTA NPs (1)	18.4/16.0	[50]
DH-DO2A NPs (2)	15.3/12.0	[50]
HCDTA/liposome (3)	17.3/16.3	[51]
tris-dipicolinate/block copolymer (4)	10.8/n.d.	[52]
pyridine-bis-hydroxyproline/polymer (5)	23.2/14.4	[53]
CDTA/SNPs (6)	18.6/7.3	[54]
EDTA/Nanodiamonds (7)	8.1/n.d.	[55]
NG-1	30.5 /16.9	This work

Their effectiveness as MRI probes is clearly highlighted by the relaxivity parameter. Indeed, the r_1 value (for Mn ion) of these new nanogels is significantly higher than that reported for many Mn(II)-based nanosystems under identical experimental conditions (Table 4 and Figure 10).

All these characteristics explain why the new nanoprobe are able to combine an improved relaxation performance with satis-

factory biocompatibility, and therefore are suitable for preclinical MRI studies in vivo. In our opinion, these results open a new avenue for the development of Mn-based nanoprobe for in vivo diagnosis with good stability and biocompatibility, good tumor accumulation capacity and excellent MRI contrast-enhancing characteristics.

4. Experimental Section

Reagents: All chemicals were purchased from Sigma–Aldrich Co. and used without further purification.

Synthesis of *t*-CDTA-Bisanhydride: 500 mg of *trans*-1,2-diaminocyclohexane-*N,N,N',N'*-tetraacetic acid (*t*-CDTA, 1.41 mmol), 2.6 mL of acetic anhydride (20 eq.) and 0.44 mL of pyridine (4 eq.) were stirred overnight, at room temperature, under inert atmosphere (N_2). The product was then precipitated by adding diethyl ether (100 mL) to the reaction mixture and separated by centrifugation at room temperature (4000 rpm for 15 min). The yellowish-white product obtained was washed for three times with 100 mL of diethyl ether. The solid was dried under vacuum to obtain 327.3 mg of *t*-CDTA-bisanhydride (yield of 72.9%).

Synthesis of Mono- and bis-*t*-CDTA-Glucosamide (*t*-CDTAGlu₁ and *t*-CDTAGlu₂): 260 mg of *t*-CDTA-bisanhydride (0.81 mmol) were first dispersed in 5 mL of anhydrous dimethylacetamide (DMA); separately, 723 mg of D-(+)-Glucosamine hydrochloride (4 eq.) was solubilized in 5 mL of DMSO. The D-(+)-Glucosamine hydrochloride solution was then added dropwise to the *t*-CDTA-bisanhydride solution, and the mixture was stirred for 3 days at 348 K under inert atmosphere. Afterward, the product

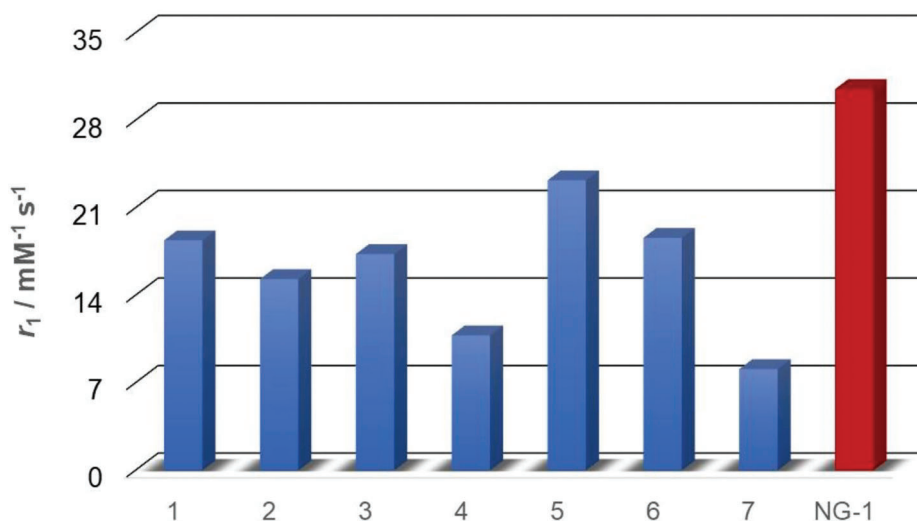


Figure 10. r_1 values (per Mn; 0.5 T and 298 K) of Mn-NG-1 and different nanoparticles functionalized with Mn(II) chelates (see data listed in Table 4).

was precipitated in diethyl ether (100 mL) and separated by centrifugation at RT (4000 rpm for 15 min): the brown product obtained was washed for three times with 100 mL of diethyl ether. *t*-CDTAGlu₁ and *t*-CDTAGlu₂ were then purified by semi-preparative HPLC-MS (400 μL of a 10 mg mL⁻¹ solution in H₂O, flow 20 mL min⁻¹) using an Atlantis TM Prep dC18 5 μm OBDMT 19 \times 100 mm (Waters), by using the method reported in the ESI (Table S2, Supporting Information).

Yield of *t*-CDTAGlu₁: 72 mg, 18%.

Yield of *t*-CDTAGlu₂: 49 mg, 9%.

t-CDTAGlu₁: MS ESI⁻ (m/z) = 509.3 [M+H⁺]; calculated for C₂₀H₃₃N₃O₁₂ = 508.18. In the ¹H and ¹³C NMR spectra duplicated signals were observed due to the α and β anomers of the glucosamine: asterisk indicates protons corresponding to the α anomer (Figures S10 and S11, Supporting Information). ¹H-NMR (D₂O, 500 MHz, 300 K) δ = 5.18* (0.5 H -NH-CH-CH-OH, glucosamide), 5.11 (0.5 H -NH-CH-CH-OH, glucosamide), 4.02-3.27 (-CH₂-COOH, 6H, and glucosamide, 6H), 3.22-3.05 (-N-CH-CH-N-, 2H, cyclohexyl), 2.11 (CH₂, 2H, cyclohexyl), 1.78 (CH₂, 2H, cyclohexyl), 1.46-1.10 (CH₂, 4H, cyclohexyl). ¹³C-NMR (D₂O, 125 MHz, 300 K) δ = 174.1 (-COOH), 173.7 (-CONH), 94.7 (-CH-OH), 90.8* (-CH-OH), 76.0* (-CH-OH), 73.8 (-CH-OH), 71.5 (-CH-CH₂-OH), 70.1* (-CH-CH₂-OH), 70.0 (-CH-OH), 69.7* (-CH-OH), 63.0 (-NH-CH-CH-NH-, cyclohexyl), 60.8* (-CH-CH₂-OH), 60.6 (-CH-CH₂-OH), 56.9 (-CH₂-CONH-), 56.8 (-CH-NH-), 54.2 (-CH₂-COOH), 54.1* (-CH-NH-), 23.8 (-CH₂-CH₂-CH₂-CH₂, cyclohexyl), 20.4 (-CH₂-CH₂-CH₂-CH₂, cyclohexyl).

t-CDTAGlu₂: MS ESI⁻ (m/z) = 669.6 [M+H⁺]; calculated for C₂₆H₄₄N₄O₁₆ = 668.26. ¹H NMR (D₂O) (Figure S12, Supporting Information): 5.19* (-NH-CH-CH-OH, 1H, glucosamide), 5.12 (-NH-CH-CH-OH, 1H, glucosamide), 4.03-3.30 (-CH₂-COOH, 4H and glucosamide, 12H), 3.24-3.08 (-N-CH-CH-N-, 2H, cyclohexyl), 2.11 (CH₂, 2H, cyclohexyl), 1.78 (CH₂, 2H, cyclohexyl), 1.42-1.12 (CH₂, 4H, cyclohexyl). ¹³C NMR (D₂O, 125 MHz, 300 K) (Figure S13, Supporting Information): 174.1 (-COOH), 173.9 (-CONH), 94.4 (-CH-OH), 90.8* (-CH-OH), 76.0* (-CH-OH), 73.9 (-CH-OH), 71.4 (-CH-CH₂-OH), 70.8* (-CH-CH₂-OH), 70.0 (-CH-OH), 69.8* (-CH-OH), 64.1 (-NH-CH-CH-NH-, cyclohexyl), 60.7* (-CH-CH₂-OH), 60.6 (-CH-CH₂-OH), 56.8 (-CH₂-CONH-), 56.6 (-CH-NH-), 54.3 (-CH₂-COOH), 54.2* (-CH-NH-), 23.9 (-CH₂-CH₂-CH₂-CH₂, cyclohexyl), 20.2 (-CH₂-CH₂-CH₂-CH₂, cyclohexyl).

Mn-t-CDTAGlu₁ and *Mn-t*-CDTAGlu₂: *t*-CDTAGlu₁ (10 mg, 0.015 mmol) was dissolved in 1 mL of pure water. A slight stoichiometric excess (\approx 5%) of MnCl₂•6H₂O was added, and the solution was stirred at room temperature overnight, maintaining the pH \approx 4 with a diluted NaOH solution (0.5 M). The pH of the solution was then increased to 9.5 to promote the precipitation of the excess of Mn(II) as hydroxide. The suspension was filtered through a 0.2 μm filter and neutralized with

diluted HCl. MS ESI⁻ (m/z) = 559.5 [M]⁻; calculated C₂₀H₃₀MnN₃O₁₂ = 559.1.

Mn-t-CDTAGlu₂ was prepared following the same experimental procedure. MS ESI⁺ (m/z) = 722.2 [M+H⁺]; calculated C₂₆H₄₂MnN₄O₁₆ = 721.2.

Nanogel (NG-1): The nanogel was prepared by adapting a procedure reported in the literature.^[29] In detail, 21 mg of chitosan (Sigma-Aldrich 523682-1G) were dissolved in 2 mL of ultrapure water: in parallel, 92 mg (0.297 mmol) of *t*-CDTA-bisanhydride were dispersed in 8 mL of anhydrous DMA. The chitosan solution was added dropwise to the *t*-CDTA-bisanhydride suspension and the mixture was stirred overnight at room temperature to promote the complete formation of the nanoparticles. The suspension was centrifuged (7000 rpm \times 15 min) to remove the solvent, and the solid was re-suspended in 10 mL of NaOH 0.01 M. The final suspension was purified by dialysis with a membrane with cut off of 1000 Da in basic, acid and neutral aqueous solutions. Following the same approach, nanogels with double (0.594 mmol) and one-third (0.099 mmol) amount of *t*-CDTA-bisanhydride were also prepared (NG-2 and NG-1/3, respectively).

The water content in the nanogel was quantified by gravimetric approach: 1 mL of the nanogel suspension was left in the oven at 343 K until evaporation of the solvent to obtain the hydrated solid, and then weighted. Afterward, the powder was dehydrated completely at 373 K for 24 h and weighted again. The amount of entrapped water was calculated by applying the following equation:

$$\text{water amount (\%)} = \frac{m_{\text{NG}}^{\text{wet}} - m_{\text{NG}}^{\text{dried}}}{m_{\text{NG}}^{\text{wet}}} \times 100 \quad (2)$$

The functionalization degree of chitosan after reaction with *t*-CDTA-bisanhydride was determined by ninhydrin assay by adapting a method reported in the literature.^[30] The ninhydrin reagent was prepared by dissolving 0.5 g of ninhydrin and 15 mg of ascorbic acid in 60 mL of DMSO. 1.5 mL of freshly prepared ninhydrin reagent solution was mixed with 0.5 mL of nanogel. The mixture was heated at 373 K for 20 min, cooled down to room temperature prior to UV measurement. The amount of free amino groups in the sample can be quantified by analyzing absorbance of the band at 570 nm. A calibration curve was carried out by monitoring the absorbance of different amounts of D-(+)-Glucosamine (standard reactant) after reaction with ninhydrin solution.

Mn-NG-1. The manganese complexation of NG was followed by relaxometric titration. The titration was performed at 10 MHz and 298 K, by adding increasing amount of MnCl₂ solution (48.44 mM) to 4.5 mL of NG

suspension and maintaining the pH at 4.5. R_1 values were measured after each addition of Mn(II) solution. The excess of metal was removed by adding at the end of titration 0.7 mL of NG suspension. The same procedure was also adopted to prepare Mn-NG-3 sample.

Characterization Techniques: Electrospray ionization mass spectra (ESI MS) were recorded using an SQD 3100 Mass Detector (Waters), operating in positive- or negative-ion mode, with 1% v/v formic acid in methanol as the carrier solvent.

^1H and ^{13}C NMR spectra of the ligands and their precursors were recorded at 298 K using a Bruker AVANCE III 500 spectrometer equipped with a wide bore 11.7 Tesla magnet. The Mn(II) concentration in the aqueous suspensions was determined by ^1H NMR measurements using the Bulk Magnetic Susceptibility (BMS) method.^[56]

IR spectra were recorded in the 4000–400 cm^{-1} range using a Bruker Equinox 55 spectrometer. Prior to the analysis, the samples were mixed with KBr matrix.

Cryo-transmission electron microscopy (cryo-TEM) micrographs were obtained by using a Thermo Scientific Glacios electron microscope equipped with a 200 kV X-FEG optics. The sample was prepared in a Vitro-robot chamber at room temperature and then deposited in a carbon-film grid and vitrified in liquid ethane at its freezing point.

Dynamic light scattering (DLS) and Z-potential experiments were carried out at 298 K by using a Malvern Zetasizer NanoZS operating in a particle size range from 0.6 nm to 6 μm and equipped with a He-Ne laser with $\lambda = 633$ nm.

$1/T_1$ ^1H Nuclear Magnetic Relaxation Dispersion (NMRD) profiles were measured on a Fast-Field Cycling (FFC) Stellar SmarTracer Relaxometer over a continuum of magnetic field strengths from 0.00024 to 0.25 T (0.01–10 MHz proton Larmor Frequencies). The relaxometer operates under computer control with an absolute uncertainty in $1/T_1$ of $\pm 1\%$. Data in the 20–120 MHz frequency range were collected with a High Field Relaxometer (Stellar) equipped with the HTS-110 3T Metrology Cryogen-free Superconducting Magnet. The temperature was controlled during the measurements with a Stellar VTC-91 airflow heater equipped with a copper-constantan thermocouple (uncertainty of $\pm 0.1\%^\circ\text{C}$). Furthermore, the real temperature inside the probe head was monitored by a Fluke 52k/j digital thermometer (Fluke, Zürich, Switzerland). The data were collected using the standard inversion recovery sequence (20 experiments, 2 scans) with a typical 90° pulse width of 3.5 μs , and the reproducibility of the data was within $\pm 0.5\%$. The diamagnetic contribution was measured by collecting ^1H NMRD profiles of the unloaded nanoparticles, at different temperatures. The relaxivity (r_1 , $\text{mM}^{-1} \text{s}^{-1}$) at different magnetic fields and temperatures was obtained by measuring the longitudinal relaxation rates of the paramagnetic suspensions, subtracting the diamagnetic contribution of nanogel, and normalizing the final value to mM concentration of Mn(II).

Variable ^{17}O NMR measurements were recorded on a Bruker Avance III spectrometer (11.7 T) equipped with a 5 mm probe and a Bruker BVT 3200 control unit. Aqueous solutions of the samples at physiological pH (7.4) and containing 2.0% of the ^{17}O isotope (Cambridge Isotope) were used.

In Vitro Experiments: In vitro experiments were carried out on the murine macrophage cell line RAW 264.7 (ATCC, LGC Standards, Sesto San Giovanni, Italy). The cells were cultured in DMEM (Lonza, Basel, Switzerland) supplemented with 10% (v/v) FBS, 2 mM L-glutamine, 100 U mL^{-1} penicillin and 100 $\mu\text{g mL}^{-1}$ streptomycin at 37°C in a humidified atmosphere with 5% CO_2 . For the MTT (3-(4,5-dimethylthiazol-2-yl)-2,5-diphenyl-2H-tetrazolium bromide) assay the cells were plated in a 96-well plate (5×10^4 cells/well). The day after the cells were incubated with increasing amounts of Mn-NG-1 in complete culture medium (corresponding to a final Mn(II) concentration of 0, 10, 25, 50, 100, 250, or 500 μM) for 24 h at 37°C in a humidified atmosphere with 5% CO_2 . Then the cells were profusely washed with PBS and the MTT assay was carried out with the MTT cell proliferation kit (OZ biosciences SAS, Marseille, France), according to the protocol reported in the datasheet (2 h MTT incubation). The viability was expressed as a percentage of control (non-incubated) cells.

In Vivo Experiments: In vivo experiments were carried out on BALB/c male mice (8–12 weeks old) obtained from the animal facility of the Molec-

ular Biotechnology Center (MBC) of the University of Turin (Italy). Experiments were performed according to the national laws on animal experimentation and approved by the Italian Ministry of Health. Mice were kept in standard housing with standard rodent chow and water available ad libitum, and a 12 h light/dark cycle. Mice were anesthetized by intramuscular injection of a combination of 20 mg kg^{-1} tiletamine/zolazepam (Zoletil 100; Virbac, Milan, Italy) and 5 mg kg^{-1} xylazine (Rompun; Bayer, Milan, Italy). Before injection, the nanogels were diluted in HEPES/NaCl buffer to obtain an isotonic suspension (300 mOsm, 2 mM Mn(II) concentration).

In Vivo Experiments—Blood Half-Life Time of Mn-NG-1: The blood half-life time of Mn-NG-1 based nanogel was investigated in healthy BALB/c male mice ($n = 3$). The nanogel was intravenously administered (13 $\mu\text{mol Mn(II)/kg bw}$) in the tail vein. Then, at different time points (5, 15, 30 min, and 1, 2, 4, 6.5, 26 h), a micro aliquot of blood was collected from the tail vein. An aliquot of blood was also collected before the experiment, to determine the physiological Mn(II) blood content in each mouse. 20 μL of Heparin (500 UI mL^{-1}) were added to each sample to avoid coagulation. To quantify the amount of Mn(II), the exact volume of blood collected at each time was quantified through ICP-MS (see paragraph below). The data obtained were reported as the mean ng of Mn(II)/ μL blood \pm standard deviation (SD) versus time post-injection and fitted with an exponential decay curve, to calculate the blood half-life time.

In Vivo Experiments—ICP-MS Quantification of Mn(II) Content: The Mn(II) content in blood and excised organs and tissues was measured by Inductively Coupled Plasma Mass Spectrometry (ICP-MS) analysis (Element-2; Thermo-Finnigan, Rodano (MI), Italy) and the results expressed as $\mu\text{g/g}$ of wet tissue weight or ng Mn(II)/ μL blood. The preparation of the samples for ICP-MS analysis was carried out as follows: 1 mL (2 mL in the case of liver tissues) of nitric acid (HNO_3) 70% for trace metal analysis (Thermo ScientificTM, USA) was added to the samples. After 3–5 days, the completely dissolved materials were further mineralized under microwave heating at 180°C for 35 min (Milestone ETHOS UP High-performance Microwave digestion system equipped with an optical fiber, temperature control, and SK-15 high-pressure rotor, Bergamo, Italy). After mineralization, the volume of each sample was brought to 3 mL with ultrapure water and the samples were analyzed by ICP-MS. The calibration curve was obtained using four absorption standard solutions (Sigma-Aldrich) containing equimolar concentrations of Mn(II) in the range of 0.005–0.1 $\mu\text{g mL}^{-1}$.

In Vivo Experiments—MRI In Vivo Experiments: For MRI in vivo experiments, a mouse model of breast cancer was used. The model was obtained by inoculating 3×10^5 TS/A mouse mammary adenocarcinoma cells subcutaneously in both flanks of female BALB/c mice ($n = 3$). After 2 weeks the mice were recruited for the study. Animals were anesthetized as previously reported, placed supine in a solenoid Tx/Rx coil with an inner diameter of 3.5 cm, and a catheter was inserted into their tail vein. A standard reference tube containing Prohance 0.1 mm was placed next to the mouse for normalization of signal intensity. Then, MR images of the spleen, liver, tumor, and kidneys were acquired at 1T with the Aspect M2 MRI System (Aspect Magnet Technologies Ltd. Netanya, Israel), before, dynamically for 27 min, and then 0.5, 4, 24, and 48 h post-injection of the Mn-NG-1 nanogel (13 $\mu\text{mol Mn(II)/kg bw}$). A Fast Spin Echo (FSE) sequence was used for the T_2 weighted (T_{2w}) acquisitions with the following parameters: Repetition Time (T_R)/ Echo Time (T_E)/ Number of Experiments (N_{EX}) 2500/49/4, Field of View (FOV) = 40 mm, number of slices 4, inter-slice gap 0.1 mm, slice thickness 2 mm, acquisition time 2 m 50 s. Dynamic Contrast Enhanced (DCE)-MRI was performed using an axial Gradient Echo (GRE) SNAP sequence (TR 16 ms; TE 2.7 ms; flip angle 30° ; number of slices 4; slice thickness 2.0 mm; slice gap 0.1 mm; FOV 40 mm; matrix 128×128 ; NEX 5; temporal resolution 42 s per image). The dynamic series was acquired with three initial pre-contrast T_{1w} images and 37 dynamic post-contrast images for a total examination time of 27 min. Before the nanogel administration, a variable flip angle (VFA) map was acquired with the GRE SNAP sequence: NAV 5, 1 repetition, flip angle 5-15-30-45-60-75°. T_{1w} images were acquired with the same GRE SNAP sequence of DCE, but with NEX = 15, acquisition time 3 min 12 s.

Image analysis and statistics were performed using Fiji free software. The mean signal intensity (SI) values were calculated on the regions

of interest (ROI). The measured SI was normalized with the standard reference tube (ref) in each slice as follows:

$$SI_{norm} = \frac{SI_{ROI}}{SI_{ref}} \quad (3)$$

Then the % T₁ Signal Enhancement (% T₁ SE) over pre-images was calculated at each time t post nanogel injection as follows:

$$\%T_1SE = \frac{SI_{norm\ t} - SI_{norm\ pre}}{SI_{norm\ pre}} \times 100 \quad (4)$$

Results obtained were expressed as mean % T₁ SE values ± SD.

In Vivo Experiments—Ex-Vivo Experiments: To quantify the Mn(II) content in each organ by ICP-MS, 6 female mice were inoculated with TS/A cells and recruited after two weeks. Then, mice (n = 3) were sacrificed, and the organs were collected to determine the basal content of Mn(II) in the spleen, tumor, liver, and kidneys. Another mice group of the same size (n = 3) was sacrificed 24 h post-injection of the Mn-NG-1 nanogel and the organs were collected. The exact weight of each organ was determined, then 1 mL (2 mL in the case of liver tissues) of HNO₃ 70% for trace metal analysis was added to the samples and the organs were processed as reported above. Results obtained were reported as the mean µg of Mn(II)/g of wet tissue weight + SD.

Statistical Analysis: The experimental data are reported as mean ± SD or SME. The sample size for each statistical analysis is included in the caption of the Figures. Origin 2021 and GraphPad Prism Version 5.03 were used for the statistical analysis.

Supporting Information

Supporting Information is available from the Wiley Online Library or from the author.

Acknowledgements

The authors acknowledge the Fondazione Cassa di Risparmio di Firenze, the PRIN 2017A2KEPL project “Rationally designed nanogels embedding paramagnetic ions as MRI probes”, and the European Commission through H2020 FET-Open project HIREM-MULTIDYN (grant agreement no. 899683) for the financial support. The authors acknowledge the support and the use of resources of Instruct-ERIC, a landmark ESFRI project, and specifically the CERM/CIRMMP Italy center and the FloCEN laboratory within Instruct-ITALIA (PID: ITA026).

Conflict of Interest

The authors declare no conflict of interest.

Author Contributions

M.B., C.L. and E.T. performed conceptualization, project administration and supervised. M.B., C.L., E.T. performed funding acquisition. F.C., L.T., G.P., F.G. performed investigation and methodology. M.R., F.G., C.F., G.P. performed formal analysis. All authors performed visualization, and part contributions to manuscript. F.C., M.R., L.T., G.P., M.B. wrote the original draft. C.L., E.T. wrote, reviewed and all authors finalize the manuscript.

Data Availability Statement

The data that support the findings of this study are available from the corresponding author upon reasonable request.

Keywords

contrast agents, manganese(II), magnetic resonance imaging (MRI), nanogels, relaxometry, water exchange

Received: April 5, 2023

Revised: June 1, 2023

Published online:

- [1] J. Wahsner, E. M. Gale, A. Rodríguez-Rodríguez, P. Carvan, *Chem. Rev.* **2019**, *119*, 957.
- [2] P. Caravan, J. J. Ellison, T. J. McMurry, R. B. Lauffer, *Chem. Rev.* **1999**, *99*, 2293.
- [3] S. Aime, M. Botta, E. Terreno, *Adv. Inorg. Chem.* **2005**, *57*, 173.
- [4] S. H. Koenig, R. D. Brown, *Prog. Nucl. Magn. Reson. Spectrosc.* **1990**, *22*, 487.
- [5] L. Helm, J. R. Morrow, C. J. Bond, F. Carniato, M. Botta, M. Braun, Z. Baranyai, R. Pujales-Paradela, M. Regueiro-Figueroa, D. Esteban-Gomez, C. Platas-Iglesias, T. J. Scholl, in *Contrast Agents for MRI: Experimental Methods*, The Royal Society of Chemistry, Cambridge (UK) **2018**, Ch. 2.
- [6] M. Botta, L. Tei, *Eur. J. Inorg. Chem.* **2012**, *2012*, 1945.
- [7] D. D. Castelli, E. Gianolio, S. G. Crich, E. Terreno, S. Aime, *Coord. Chem. Rev.* **2008**, *252*, 2424.
- [8] A. J. L. Villaraza, A. Bumb, M. W. Brechbiel, *Chem. Rev.* **2010**, *110*, 2921.
- [9] X. Mao, J. Xu, H. Cui, *Wiley Interdiscip. Rev.: Nanomed. Nanobiotechnol.* **2016**, *8*, 814.
- [10] F. Carniato, L. Tei, M. Botta, *Eur. J. Inorg. Chem.* **2018**, *2018*, 4936.
- [11] W.-Y. Huang, G.-L. Davies, J. J. Davis, *Chem. Commun.* **2013**, *49*, 60.
- [12] T. R. Berki, J. Martinelli, L. Tei, H. Willcock, S. J. Butler, *Chem. Sci.* **2021**, *12*, 3999.
- [13] M. Callewaert, V. G. Roullin, C. Cadiou, E. Millart, L. Van Gulik, M. C. Andry, C. Portefaix, C. Hoeffel, S. Laurent, L. V. Elst, R. Muller, M. Molinari, F. Chuburu, *J. Mater. Chem. B* **2014**, *2*, 6397.
- [14] T. Courant, V. G. Roullin, C. Cadiou, M. Callewaert, M. C. Andry, C. Portefaix, C. Hoeffel, M. C. de Goltstein, M. Port, S. Laurent, L. Vander Elst, R. Muller, M. Molinari, F. Chuburu, *Angew. Chem., Int. Ed.* **2012**, *51*, 9119.
- [15] G. Rigaux, C. V. Gheran, M. Callewaert, C. Cadiou, S. N. Voicu, A. Dinischiotu, M. C. Andry, L. Vander Elst, S. Laurent, R. N. Muller, A. Berquand, M. Molinari, S. Huclier-Markai, F. Chuburu, *Nanotechnology* **2016**, *28*, 055705.
- [16] F. Carniato, L. Tei, M. Botta, E. Ravera, M. Fragai, G. Parigi, C. Luchinat, *ACS Appl. Bio. Mater.* **2020**, *3*, 9065.
- [17] M. Chan, J. Lux, T. Nishimura, K. Akiyoshi, A. Almutairi, *Biomacromolecules* **2015**, *16*, 2964.
- [18] F. Carniato, M. Ricci, L. Tei, F. Garello, E. Terreno, E. Ravera, G. Parigi, C. Luchinat, M. Botta, *Inorg. Chem.* **2022**, *61*, 5380.
- [19] E. Rosa, F. Carniato, L. Tei, C. Diaferia, G. Morelli, M. Botta, A. Accardo, *Pharmaceuticals* **2022**, *15*, 1572.
- [20] J. Lux, M. Chan, L. Vander Elst, E. Schopf, E. Mahmoud, S. Laurent, A. Almutairi, *J. Mater. Chem. B* **2013**, *1*, 6359.
- [21] A. Soleimani, F. Martínez, V. Economopoulos, P. J. Foster, T. J. Scholl, E. R. Gillies, *J. Mater. Chem. B* **2013**, *1*, 1027.
- [22] E. Gallo, E. Rosa, C. Diaferia, F. Rossi, D. Tesauro, A. Accardo, *RSC Adv.* **2020**, *10*, 27064.
- [23] H. S. Thomsen, S. K. Morcos, P. Dawson, *Clin. Radiol.* **2006**, *61*, 905.
- [24] V. Gulani, F. Calamante, F. G. Shellock, E. Kanal, S. B. Reeder, *Lancet Neurol.* **2017**, *16*, 564.

- [25] K. Inoue, M. Fukushi, S. K. Sahoo, N. Veerasamy, A. Furukawa, S. Soyama, A. Sakata, R. Isoda, Y. Taguchi, S. Hosokawa, H. Sagara, T. Natarajan, *Mar. Pollut. Bull.* **2022**, *174*, 113259.
- [26] M. Botta, F. Carniato, D. Esteban-Gómez, C. Platas-Iglesias, L. Tei, *Future Med. Chem.* **2019**, *11*, 1461.
- [27] E. Molnar, B. Varadi, Z. Garda, R. Botar, F. K. Kalman, E. Toth, C. Platas-Iglesias, I. Toth, E. Brucher, G. Tircso, *Inorg. Chim. Acta* **2018**, *472*, 254.
- [28] Z. Baranyai, Z. Garda, S. Ghiani, F. K. Kalman, L. Krusper, A. Maiocchi, G. Tircso, I. Toth, *Int. Pat. Appl.* **2016**, WO2016135234A1.
- [29] X. Shen, L. Zhang, X. Jiang, Y. Hu, J. Guo, *Angew. Chem., Int. Ed.* **2007**, *46*, 7104.
- [30] S. Yokoyama, J.-I. Hiramatsu, *J. Biosci. Bioeng.* **2003**, *95*, 204.
- [31] I. Bertini, O. Galas, C. Luchinat, G. Parigi, *J. Magn. Reson., Ser. A* **1995**, *113*, 151.
- [32] G. Lipari, A. A. Szabo, *J. Am. Chem. Soc.* **1982**, *104*, 4546.
- [33] T. J. Swift, R. E. Connick, *J. Chem. Phys.* **1962**, *37*, 307.
- [34] S. Aime, A. Barge, J. I. Bruce, M. Botta, J. A. K. Howard, J. M. Moloney, D. Parker, A. S. de Sousa, M. Woods, *J. Am. Chem. Soc.* **1999**, *121*, 5762.
- [35] H. Li, G. Parigi, C. Luchinat, T. J. Meade, *J. Am. Chem. Soc.* **2019**, *141*, 6224.
- [36] P. Caravan, G. Parigi, J. M. Chasse, N. J. Cloutier, J. J. Ellison, R. B. Lauffer, C. Luchinat, S. A. McDermid, M. Spiller, T. J. McMurry, *Inorg. Chem.* **2007**, *46*, 6632.
- [37] M. Fragai, E. Ravera, F. Tedoldi, C. Luchinat, G. Parigi, *ChemPhysChem* **2019**, *20*, 2204.
- [38] A. T. Preslar, G. Parigi, M. T. McClendon, S. S. Seifick, T. J. Moyer, C. R. Haney, E. A. Water, K. W. MacRenaris, C. Luchinat, S. I. Stupp, T. J. Meade, *ACS Nano* **2014**, *8*, 7325.
- [39] F. Alhaique, I. Bertini, M. Fragai, M. Carafa, C. Luchinat, G. Parigi, *Inorg. Chim. Acta* **2002**, *331*, 151.
- [40] J. A. Peters, C. F. G. C. Geraldes, *Inorganics* **2018**, *6*, 116.
- [41] I. V. Zelepukin, A. V. Yaremenko, M. V. Yuryev, A. B. Mirkasymov, I. L. Sokolov, S. M. Deyev, P. I. Nikitin, M. P. Nikitin, *J. Controlled Release* **2020**, *326*, 181.
- [42] W. Lu, J. Wan, Z. She, X. Jiang, *J. Controlled Release* **2007**, *118*, 38.
- [43] M. P. Federle, J. L. Chezmar, D. L. Rubin, J. C. Weinreb, P. C. Freeny, R. C. Semelka, J. J. Brown, J. A. Borrello, J. K. T. Lee, R. Mattrey, A. H. Dachman, S. Saini, B. Harmon, M. Fenstermacher, R. E. Pelsang, S. E. Harms, D. G. Mitchell, H. H. Halford, M. W. Anderson, C. D. Johnson, I. R. Francis, J. G. Bova, P. J. Kenney, D. L. Klippenstein, G. S. Foster, D. A. Turner, A. E. Stillman, R. C. Nelson, S. W. Young, R. H. Patt, et al., *J. Magn. Reson. Imaging* **2000**, *12*, 186.
- [44] D. Pan, A. H. Schmieder, S. A. Wickline, G. M. Lanza, *Tetrahedron* **2011**, *67*, 8431.
- [45] K. G. Toft, S. O. Hustvedt, D. Grant, G. A. Friisk, T. Skotland, *Eur. J. Drug Metab. Pharmacokinet.* **1997**, *22*, 65.
- [46] A. K. Iyer, G. Khaled, J. Fang, H. Maeda, *Drug Discovery Today* **2006**, *11*, 812.
- [47] S. Nie, *Nanomedicine* **2010**, *5*, 523.
- [48] L. Zhang, Z. Cao, Y. Li, J. R. Ella-Menye, T. Bai, S. Jiang, *ACS Nano* **2012**, *6*, 6681.
- [49] H. H. Gustafson, D. Holt-Casper, D. W. Grainger, H. Ghandehari, *Nano Today* **2015**, *10*, 487.
- [50] G. A. Rolla, V. De Biasio, G. B. Giovenzana, M. Botta, L. Tei, *Dalton Trans.* **2018**, *47*, 10660.
- [51] G. Mulas, G. A. Rolla, C. F. G. C. Geraldes, L. W. E. Starmans, M. Botta, E. Terreno, L. Tei, *ACS Appl. Bio. Mater.* **2020**, *3*, 2401.
- [52] J. Wang, J. Wang, P. Ding, W. Zhou, Y. Li, M. Drechsler, X. Guo, A. M. A. C. Stuart, *Angew. Chem., Int. Ed.* **2018**, *57*, 12680.
- [53] X. Liu, S. Fu, C. Xia, M. Li, Z. Cai, C. Wu, F. Lu, J. Zhu, B. Song, Q. Gongde, H. Ai, *J. Mater. Chem. B* **2022**, *10*, 2204.
- [54] D. Lalli, G. Ferrauto, E. Terreno, F. Carniato, M. Botta, *J. Mater. Chem. B* **2021**, *9*, 8994.
- [55] W. Hou, T. B. Toh, L. N. Abdullah, T. W. Z. Yvonne, K. J. Lee, I. Guenther, E. K.-H. Chow, *Nanomedicine: Nanotech. Biol. Med.* **2017**, *13*, 783.
- [56] D. F. Evans, *J. Chem. Soc.* **1959**, 2003.